Efficient Color-Tunable Multiexcitonic Dual Wavelength Emission from Type II Semiconductor Tetrapods

Wen-Ya Wu,[†,∥] Mingjie Li,[†,∥] Jie Lian,[‡] Xiangyang Wu,[§] Edwin K. L. Yeow,[§] Mark H. Jhon,[⊥] and Yinthai Chan[†,‡,*]

[†]Department of Chemistry, National University of Singapore, 3 Science Drive 3, Singapore 117543, Singapore, [‡]Institute of Materials Research & Engineering A*STAR, 3 Research Link, Singapore 117602, Singapore, [§]Division of Chemistry and Biological Chemistry, School of Physical and Mathematical Sciences, Nanyang Technological University, 21 Nanyang Link, Singapore 637371, Singapore, and [⊥]Institute of High Performance Computing 1 Fusionopolis Way, Singapore 138632, Singapore. [∥]These authors contributed equally.

ABSTRACT We synthesized colloidal InP/ZnS seeded CdS tetrapods by harnessing the structural stability of the InP/ZnS seed nanocrystals at the high reaction temperatures needed to grow the CdS arms. Because of an unexpected Type II band alignment at the interface of the InP/ZnS core and CdS arms that enhanced the occurrence of radiative excitonic recombination in CdS, these tetrapods were found to be capable of exhibiting highly efficient multiexcitonic dual wavelength emission of equal intensity at spectrally distinct wavelengths of ∼485 and ∼675 nm. Additionally, the Type II InP/ZnS seeded CdS tetrapods displayed a wider range of pump-dependent emission color-tunability (from red to white to blue) within the context of a CIE 1931 chromaticity diagram and possessed higher photostability due to suppressed multiexcitonic Auger recombination when compared to conventional Type I CdSe seeded CdS tetrapods. By employing time-resolved spectroscopy measurements, we were able to attribute the wide emission color-tunability to the large valence band offset between InP and CdS. This work highlights the importance of band alignment in the synthetic design of semiconductor nanoheterostructures, which can exhibit color-tunable multiwavelength emission with high efficiency and photostability.
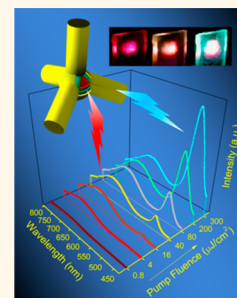
KEYWORDS: InP/CdS · Type II · tetrapod · dual-emission · multiexciton · color-tunable

Multiwavelength multiexciton emission (MME) in strongly quantum confined semiconductor nanoparticles may be broadly defined as a process in which excitons of different energies radiatively recombine within the same nanoparticle to give spectrally distinct emission wavelengths. This can be attractive for applications in which more than one emission color is desirable, such as multiplexed fluorescence labeling schemes[1−5] or ratiometric sensing in which the ratio of emission intensities of at least two resolvable wavelengths provides a means of quantifying changes in the chemical environment.[6−9] Unlike typical multiwavelength emitting nanoparticle−dye or nanoparticle−nanoparticle conjugates that suffer from a statistical distribution of stoichiometries between each type of chromophore in the conjugate, the different wavelengths of emission in the MME process originate from the same nanoparticle, thereby offering the possibility of quantitative ratiometric sensing at the single particle level. Additionally, whereas the integrated emission intensities of the different wavelengths differ as the excitation fluence is changed, MME offers a convenient means to dynamically modify the overall color of emission (as perceived by eye) from the nanoparticles by simply varying the pump intensity. It is therefore desirable to develop an architecture in which MME can be produced efficiently and with wide pump-dependent color tunability.

One method for achieving MME is *via* the use of heterostructured semiconductor nanoparticles such as CdSe seeded CdS tetrapods, where it was previously shown by Lutich et al. that saturating the CdSe core with excitons results in an "exciton-blocking" effect in which excitons generated in the CdS arms do not localize into the CdSe core but instead undergo radiative recombination. This yields steady-state PL at red and blue wavelengths from both the CdSe core and CdS arms, respectively, and it was shown that ∼55 nm long CdS arms were required to achieve effective spatial separation of the CdS exciton from the CdSe core.

Attaining equally intense emission for both core and arms in these quasi Type II semiconductor nanoheterostructures, however, required relatively high pump fluence.[10] Recent work on CdSe/CdS dot-in-a-bulk structures showed that dual emission from CdSe and CdS can be obtained at much lower pump intensities, but with limited size-dependent wavelength tunability from its bulk-like CdS shell.[11] In this work we describe a novel InP/ZnS seeded CdS tetrapod (tpod) which, by virtue of its Type II alignment and large valence band offset between the core and arms, allowed for efficient dual wavelength emission to be achieved with wider pump-dependent emission color tunability than its Type I CdSe seeded CdS counterpart. These results highlight the importance of band alignment in achieving MME in colloidal semiconductor nanostructures.

RESULTS AND DISCUSSION

The formation of monodispersed colloidal tetrapods based on II–VI semiconductors such as CdTe and CdSe via a seeded approach critically requires that the seeds possess a zinc blende (zb) or sphalerite crystal structure, which provides four out of eight ± {111} crystal facets to support the growth of the tetrapod arms.[12–14] Given that the crystal structure of InP fabricated at moderate reaction temperatures of below ~360 °C is typically that of zinc blende,[15] it is expected that colloidal InP particles should be able to serve as seeds for the heterogeneous nucleation and growth of CdS arms to yield III–V/II–VI tetrapod nanostructures with unique physicochemical properties. Our initial attempts to utilize the bare InP particles as seeds for the growth of CdS tetrapod arms, however, resulted in the severe structural degradation of InP at the high reaction temperatures required. This was overcome by the use of ZnS coated InP quantum dots (QDs) synthesized via a single pot approach. In this procedure, a mixture of In, P, Zn, and S precursors were heated up to a temperature of between 240 and 300 °C for ~1.5 h in a reaction flask containing octadecene (ODE) as the solvent and myristic acid as the capping group. This resulted in an alloyed InZnP interfacial layer between the InP core and a thin outermost ZnS shell, as previously characterized by Reiss et al.[16–18] A second ZnS shell was grown onto the as-synthesized nanocrystals mentioned above in a one-pot fashion by reintroducing the Zn and S precursors followed by annealing at 250 °C for ~30 min and 300 °C for 20 min. This was found to be necessary to achieve better surface crystallinity to support the growth of CdS arms (see Supporting Information for experimental details). Figure 1a is a typical transmission electron microscope (TEM) image of the InP/ZnS nanoparticles produced, where the average particle diameter is ~3 nm with a size dispersity of ~9%. These particles were then used as cores to support the growth of CdS. Briefly, the InP/ZnS particles were mixed with trioctylphosphine sulfide (TOPS) and injected swiftly into a cadmium precursor containing a mixture of n-trioctylphosphine oxide (TOPO), n-octadecylphosphonic acid (ODPA), and n-hexylphosphonic acid (HPA) at a temperature of ~355 °C. This resulted in uniform InP/ZnS seeded CdS tetrapod structures with CdS arm dimensions of ~5.2 nm in diameter and ~28.5 nm in length, as exemplified in Figure 1b. Analogous to the seeded growth of CdSe/CdS tetrapods, the use of ODPA and HPA as surfactants was found to be critical for tetrapod arm growth in our system.[14]

Structural characterization of the as-synthesized InP/ZnS cores and InP/ZnS seeded CdS tetrapods proceeded via high resolution transmission electron microscopy (HRTEM) and powder X-ray diffraction (XRD) measurements, which are summarized in Figures 1c-f. The XRD spectra of the InP/ZnS seeds revealed three major peaks that lie in between those corresponding to the (111), (220), and (311) facets of zb-InP and zb-ZnS, which is consistent with a InP/ZnS core−shell structure.[16] This is further supported by the HRTEM image in Figure 1c, which shows the zb-ZnS lattice fringes of its (111) plane. The exposed cubic zinc blende ±{111} facets of ZnS are atomically similar to the ±{001} facets of hexagonal (wurtzite) CdS,[19] and can therefore support growth of the CdS arms. The XRD data obtained for the InP/ZnS seeded CdS tetrapods showed a dominance of peaks corresponding to that of wurtzite (wz) CdS, which may be attributed to the fact that the four CdS arms account for most of the material comprising each tetrapod. The HRTEM image of a single tetrapod, as illustrated in Figure 1d, shows that the extension of the CdS arms (fast growth) occurs along the (002) plane while increase in the arm diameter takes place along the (100) plane, which is a slow growth facet due to strongly binding alkyl phosphonic acids.[13]

To ascertain their materials composition, High-angle Annular Dark-Field Imaging Scanning TEM (HAADF-STEM) analysis and Point Energy-Dispersive X-ray Spectroscopy (EDX) were performed on individual tetrapods, as depicted in Figure 2a,b. Point EDX measurements at the central region of tetrapod, as delineated in Figure 2b, yielded a low intensity of Zn, In and P, along with comparatively strong signals from Cd and S. The Zn signal obtained using point EDX at the core region was relatively weak but was observed more prominently in area EDX, suggesting that diffusion of Zn into the CdS arms at the high reaction temperature used (as previously shown in thin film studies[20]) had occurred. This would result in a graded $Zn_xCd_{1-x}S$ core-to-arm transition, and would leave little Zn at the branch point as confirmed by point EDX analysis.

The band alignment between bulk InP and CdS is Type II, where the bands are staggered. Excitons at the InP/CdS interface are expected to exhibit spatial separation of the electron and hole wave functions: the electron is localized to CdS while the hole is
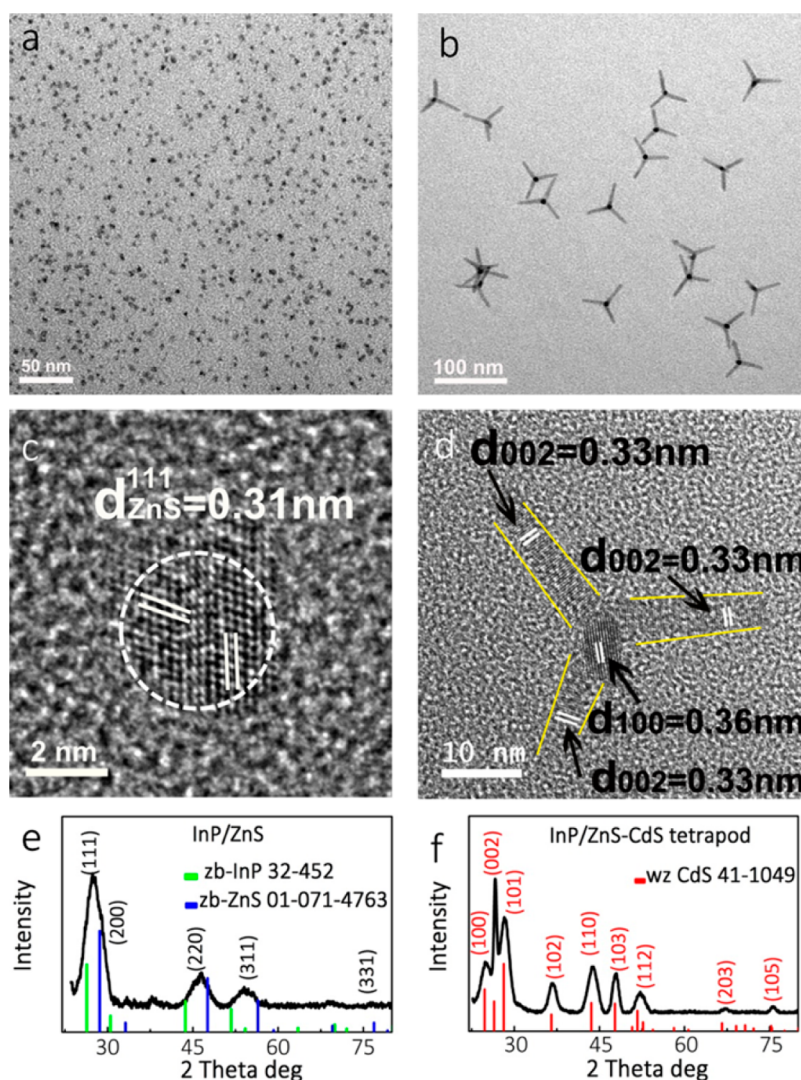
Figure 1. TEM images of as synthesized (a) InP/ZnS cores with an average diameter of ~3 nm, and (b) InP/ZnS seeded CdS tetrapods with an average arm length of ~28.5 nm and mean diameter of ~5.2 nm. (c) HRTEM image of a typical InP/ZnS seed showing lattice fringes with a *d*-spacing corresponding to the (111) plane of ZnS. (d) HRTEM image of a single tetrapod showing lattice fringes of the (100) and (002) planes corresponding to CdS. (e) Powder XRD spectrum of InP/ZnS showing peaks in-between those of standard reference zb-InP and zb-ZnS. (f) Powder XRD spectrum of InP/ZnS seeded CdS tetrapods showing the peaks of CdS wurtzite.

confined to InP.[21] However, in our InP/ZnS seeded CdS tetrapods, the interface between the InP core and CdS arms is most likely composed of an alloy of $In_yZn_{1-y}P$ and $Zn_xCd_{1-x}S$, as inferred from our structural characterization data. The consequences of the interphase structure are not immediately obvious. Whereas InP/CdS has a Type II alignment, ZnS has a Type I (straddling) alignment with both InP and CdS. Figure 2c is a cartoon depiction of the complex structural composition of a InP/ZnS seeded CdS tetrapod where we illustrated both the graded $In_yZn_{1-y}P$ layer between the InP core and ZnS shell and the $Zn_xCd_{1-x}S$ layer at the seed/arm interface. To develop an intuitive understanding of the role of an alloyed Type I interlayer on the bound states of a Type II system, we considered a simplified model. We analyzed a spherical, core–shell nanocrystal with an alloyed interlayer using an effective mass approximation.[22]

For simplicity, the hole and electron effective masses were assumed to be $m_h^* = 0.2m_0$ and $m_e^* = 0.6m_0$ in all phases. The band offsets of zb-ZnS relative to wz-CdS were taken from bulk values as $\Delta U_e^{ZnS/CdS} = 0.70$ eV and $\Delta U_h^{ZnS/CdS} = 0.40$ for electrons and holes, respectively.[23] We simulated the alloy nature of the interlayer by taking the offset of the interlayer to be proportional to the Zn content, x. The band offsets of the InP relative to the CdS were $\Delta U_e^{InP/CdS} = -0.39$ eV and $\Delta U_h^{InP/CdS} = 1.25$.[21] We calculated the ground state electron and hole radial wave functions $\mathscr{R}_e$ and $\mathscr{R}_h$ using a finite difference scheme. The time-independent radial Schrodinger equation is solved using the piecewise potential $U_i = \Delta U_i^{InP/CdS}$ for $r < R$, $U_i = x\Delta U_i^{InP/CdS}$ for $R < r < R + H_1$ and $U_i = 0$ for $R + H_1 < r < R + H_1 + H_2$, where $i = $ e,h. The e–h overlap is calculated as $\int_0^\infty r^2 \mathscr{R}_e \mathscr{R}_h \, dr$. Figure 2d illustrates the radial distribution functions $r^2\mathscr{R}_e^2$ and $r^2\mathscr{R}_h^2$ for nanocrystals with core radius 1.3 nm, interlayer
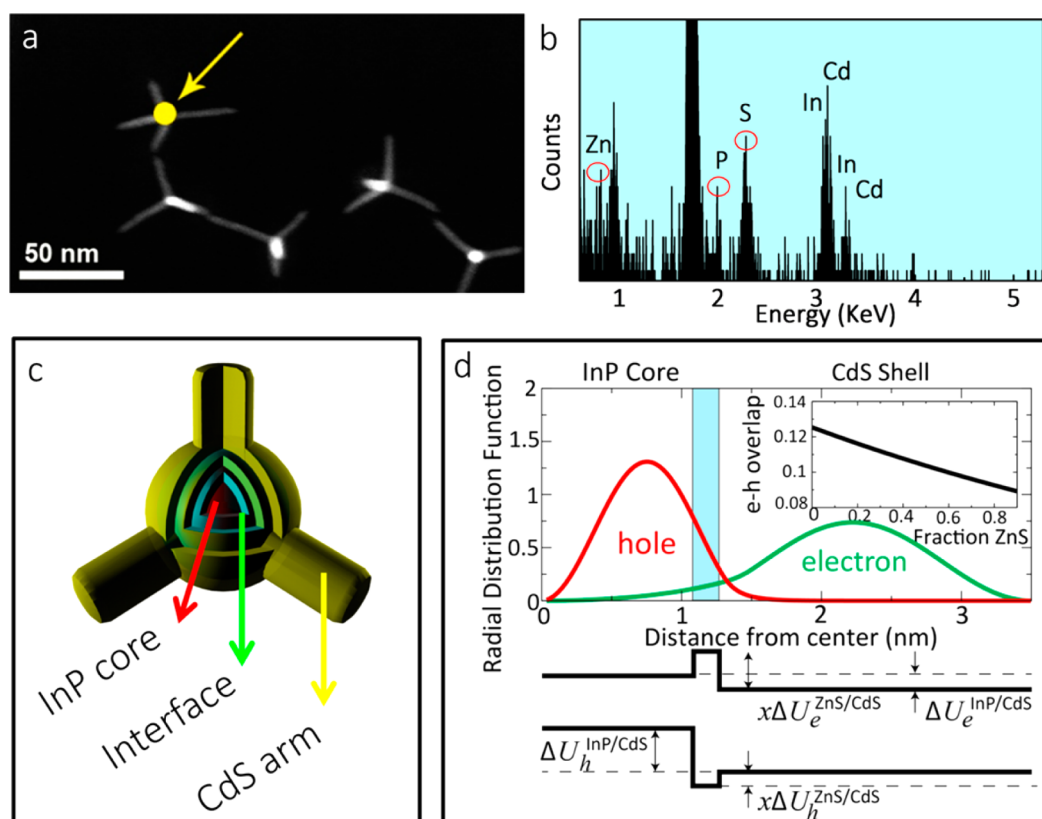
Figure 2. (a) HAADF-STEM image of InP/ZnS seeded CdS tetrapods; (b) point EDX probing the center of a single tetrapod (yellow dot in (a)), revealing signals attributed to Cd, S, In, P and Zn; (c) cartoon depicting the structure and composition of a InP/ZnS seeded CdS tetrapod; (d) e and h wave functions for a core−shell InP/CdS nanocrystal with an intermediate interlayer. The inset shows the overlap as a function of interlayer composition with respect to ZnS.

thickness 0.2 nm, and shell thickness 2 nm. From this, we conclude that the electron and hole ground state wave function overlap was very small and that the maximal overlap was at the interface. This is consistent with a Type II structure in which recombination occurs at the interface. As shown on the inset, e-h overlap decreases as the height of the barrier increases, indicating that a thin Type I barrier should not interfere with charge separation. Consequently, it may be expected that the tetrapods effectively possess a Type II alignment between its core and arms.

Optical characterization of the InP/ZnS seeded CdS tetrapods *via* absorption and PL spectrophotometry, as illustrated in Figure 3a, showed that growth of the CdS arms resulted in a CdS-dominated absorption spectrum and yielded a large emission redshift of ∼200 nm with respect to the original InP/ZnS core. The emission redshift was commensurate with an increase in the length of the CdS arms (which is inferred from comparing with core−shell InP/ZnS/CdS nanocrystals described in the Supporting Information), indicating that the observed PL was not due to deep trap emission from CdS. The absolute QY (Quantum Yield) of the tetrapods at an excitation wavelength of 400 nm was determined to be ∼20%, which is reasonable if one considers that the electron wave function is delocalized into four CdS arms which are not themselves

passivated by an inorganic shell. Time-resolved PL measurements on the InP/ZnS seeds as depicted in Figure 3b revealed a weighted-average fluorescence lifetime of ∼74 ns, whereas that of InP/ZnS seeded CdS tetrapods showed a dramatically prolonged weighted-average lifetime of ∼545 ns. These observations collectively support the notion that the tetrapods possess a Type II alignment between the core and arms, which is consistent with the prediction based on calculation.

It was also observed that the emission at ∼700 nm was blue-shifted with increasing pump fluence as shown in Figure 3c. The continuous spectral shift cannot be ascribed to the repulsive interaction between photogenerated biexcitons at high pump intensity, which would appear as an additional peak at a higher energy than that of the single exciton peak.[24,25] On the other hand, the peak energy (E_p) at excitation intensities (I_{ex}) below 60 μJ/cm^2 can be well-fitted (solid line in Figure 3c) with the expression $E_p = E_0 + c\sqrt[3]{I_{ex}}$, where E_0 is the extrapolated peak energy at zero intensity excitation and c is a fitting parameter. This is indicative of band bending, which is caused by an electric field generated by the separation of opposite charges across an interface and results in an emission blue-shift.[26−28] Deviation from the fit at pump intensities much larger than 60 μJ/cm^2 may be due to the saturation of photogenerated charge carriers
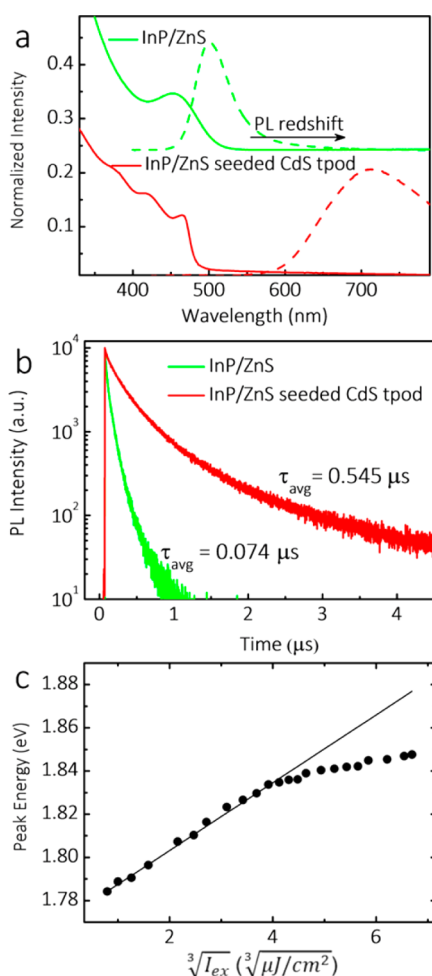
Figure 3. (a) Normalized PL (dashed lines) and UV−vis spectra (solid lines) of InP/ZnS QDs (green) and InP/ZnS-CdS tetrapods (red); (b) normalized PL decay dynamics of two samples. The average lifetime was calculated from the fitted triple-exponential decay constants weighted by their fractional amplitudes. The pump fluence is 5 μJ/cm². (c) Pump fluence dependent emission band position of InP/ZnS-CdS tetrapods.

at the interface. These observations provide further evidence that the InP/ZnS seeded CdS tetrapods exhibit Type II behavior. Upon photoexcitation, most of the excitons are generated in the CdS tetrapod arms due to their much larger absorption cross-section compared with the core at the branch point. The holes generated in the CdS arms localize to the InP core and emission takes place *via* recombination between electrons in CdS and holes in InP across the alloyed interface. Saturation of the hole states in InP would be expected to lead to radiative recombination within CdS due to the "exciton blocking effect", thus producing efficient multiexcitonic dual emission from both CdS and the InP/ZnS-CdS interface.

To better illustrate the efficiency of Type II InP/ZnS seeded CdS tetrapods in producing dual wavelength emission of similar peak intensity, a comparison was made with Type I CdSe seeded CdS tetrapods of similar CdS arm diameter and length. Both samples were excited with 400 nm pulses (1 kHz repetition rate, ∼150 fs pulse duration) from a frequency doubled

Ti:Sapphire laser. Figure 4a,b shows a series of pump intensity dependent PL spectra of dilute toluene solutions of equal concentrations of InP/ZnS seeded CdS tetrapods and CdSe seeded CdS tetrapods respectively, and it is readily seen that emission from both core and arms occurs at sufficiently large pump fluence. Their corresponding emission peak intensities as a function of the average number of photogenerated excitons per nanoparticle $\langle N \rangle$ are given in Figure 4c. It is seen that the saturation of the InP/ZnS-CdS interface emission at a pump threshold of ∼10 μJ/cm² was commensurate with a superlinear increase in the emission intensity of CdS, which may be attributed to the saturation of hole states within InP. The InP/ZnS-CdS interface emission therefore dominates at low pump fluence while the CdS emission prevails at high excitation intensities. In contrast, for the Type I tetrapods, the core CdSe emission starts to saturate at pump fluences about an order of magnitude larger without a corresponding superlinear increase in the CdS emission intensity. The sublinear increase of the CdSe core emission at large pump intensities is likely due to the Auger recombination process associated with multiexcitons[24,29] rather than core state saturation. This size-dependent Auger recombination process can also explicate the saturation of emission from the CdS arms although at larger pump fluence (∼1000 μJ/cm²) given their much larger volume.

Due to the crossover of integrated emission intensity between core and arm at a relatively low pump fluence of ∼100 μJ/cm² as illustrated in Figure 4c, InP/ZnS seeded CdS tetrapods exhibit a wide range of perceived emission color-tunability over a small excitation range. Figure 4d plots the calculated CIE coordinates according to the PL spectra in Figure 4a,b. By increasing the pump fluence gradually from 0.4 to 300 μJ/cm², the effective emission color can be tuned from red to bluish-green passing through the coordinates for white, and photographs of the Type II tetrapods dropcasted on a glass substrate optically excited under different pump intensities are given in the insets of Figure 4d. In the case of the CdSe/CdS tetrapods, the emission color has a much more limited tunability and can only be changed from red to orange with increasing pump fluence. The phostability of the Type I and Type II tetrapods as MME emitters were evaluated by monitoring their core and arm emission intensity under continuous excitation at a pump fluence of 300 μJ/cm² over the course of 1.5 h, during which no damage of the sample surfaces by the heating was observed. As illustrated in Figure 4e, the core emission intensity from the Type II tetrapods did not show any noticeable decrease whereas that of the Type I tetrapods declined appreciably over the measurement time window. This may be rationalized by the presence of a detrimental Auger recombination process in the core region of Type I tetrapods at the high pump intensities used that can result
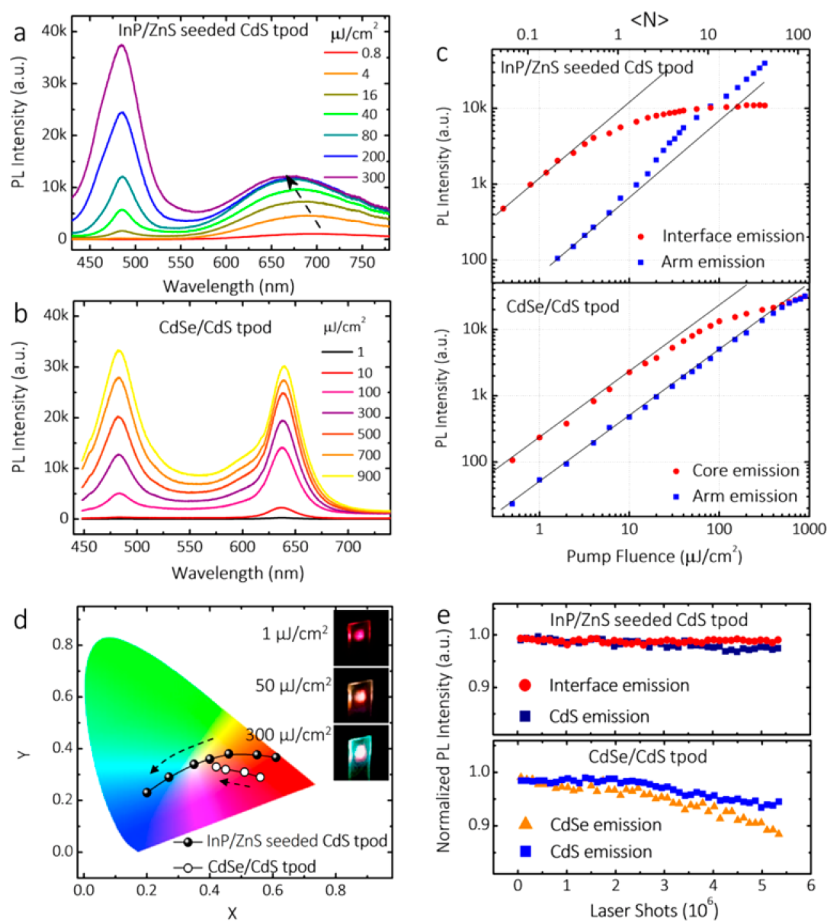
Figure 4. Pump-fluence dependent PL spectra from (a) InP/ZnS-CdS and (b) CdSe/CdS tetrapods with almost the same length of the CdS arms in the dilute toluene solution. (c) The plot of peak intensities of interface (red circles) and CdS arm (blue squares) emissions for InP/ZnS-CdS (upper panel) and CdSe/CdS tetrapods (lower panel) as a function of excitation fluence on a log–log scale in comparison to linear growth (solid line). (d) Pump-intensity dependent emission color coordinates plotted in the CIE 1931 chromaticity diagram for InP/ZnS-CdS and CdSe/CdS tetrapods. The arrows imply the increasing of pump fluence from 1 to 300 μJ/cm^2. Three inset photographs show the emission color changing of InP/ZnS-CdS tetrapods, which were drop-casted on a glass slide. (e) Emission intensity variation of Type II and Type I tetrapods upon the continuous excitation at a pump fluence of 300 μJ/cm^2 over the course of 1.5 h.

in additional occurrences of charge trapping. In the case of the Type II nanocrystals, the Auger recombination process is highly suppressed,[21,30] leading in this case to higher photostability for the Type II tetrapods.

To ascertain the origins of the early sublinear and superlinear increase in the InP/ZnS-CdS interface and CdS arm emission as a function of pump power, which is the basis for the wide color tunability obtained, the interplay of carrier dynamics between the core and arms of the tetrapod was investigated. Transient absorption (TA) measurements were performed on tetrapods to monitor their carrier relaxation and recombination processes. Figure 5a shows the differential transmission [$(T - T_0)/T_0$] spectra at a probe delay of 1 ps following a 400 nm pulse excitation for InP/ZnS seeded CdS tetrapods dispersed in toluene. Two photobleaching (PB) bands (i.e., $(T - T_0)/T_0 > 0$) denoted as X_0 and Y_0 were observed, corresponding to the transition between the InP valence band and CdS conduction band across the alloyed interface and excitonic transitions within the CdS arm. The larger amplitude

ratio of Y_0 to X_0 is due to the higher density of states and absorption cross section as a result of the much larger volume of the CdS arms in comparison with the InP core.

Figure 5b,c shows the normalized bleach decay and formation kinetics monitored at the peak of the respective X_0 and Y_0 PB bands under different pump fluence. The X_0 and Y_0 PB signals are fitted with single rising and double decaying exponential functions, respectively, as shown with solid lines. At a pump fluence corresponding to $\langle N \rangle \sim 1$ (where $\langle N \rangle$ is the average number of excitons per tetrapod), the buildup of the X_0 PB is simultaneously matched with a fast bleach decay at Y_0 PB occurring within $\sim$1.0 ps, which reflects the approximate hole relaxation time from the CdS arm to the InP core. From the amplitude of the fast decay component of Y_0 PB and its persistence beyond the fast decay component, it may be concluded that not all of the photoexcited holes are localized into the core and some holes remain within the CdS arms. This is consistent with our earlier supposition that the hole states in InP become filled and the driving force for
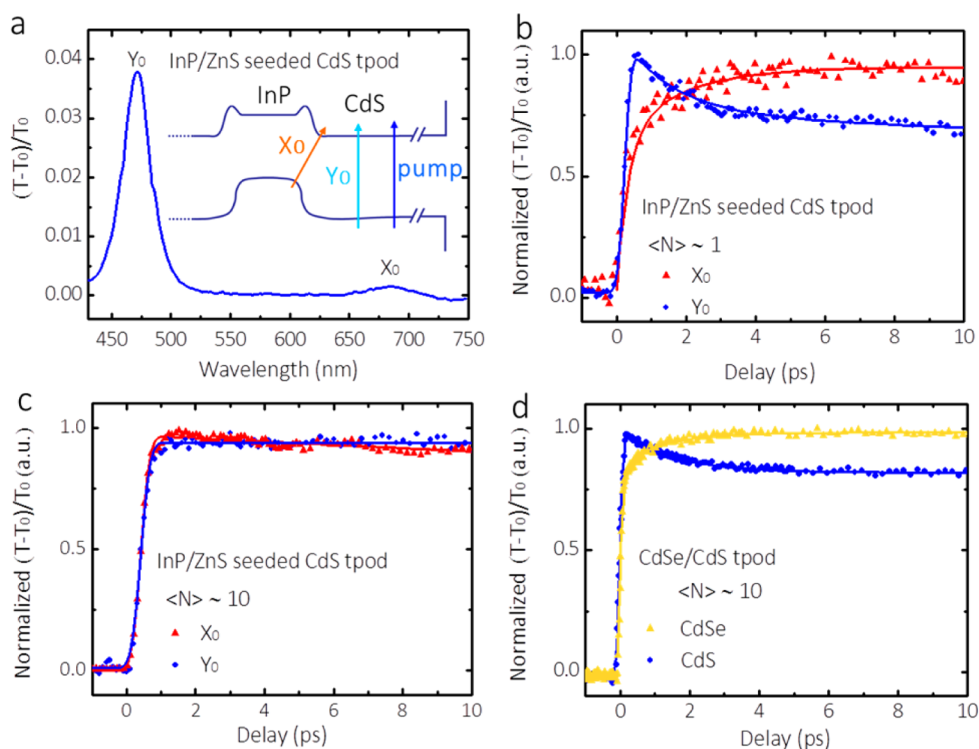
Figure 5. (a) Differential transmission spectra of InP/ZnS-CdS tetrapods dispersed in toluene at a probe delay of 1 ps under 400 nm light excitation at a pump fluence of 10 μJ/cm^2. The photobleaching (PB) bands labeled as X$_0$ and Y$_0$ correspond to the transitions across the Type II interface and in the CdS arms, respectively, as shown schematically in the inset of the energy level diagram. Normalized PB transients probed at the peaks of the X$_0$ and Y$_0$ PB bands for InP/ZnS seeded CdS tetrapods with $\langle N \rangle \sim 1$ (b) and $\langle N \rangle \sim 10$ (c). (d) Normalized PB transients probed at the peaks of the CdSe and CdS transitions for the counterpart Type I tetrapods with $\langle N \rangle \sim 10$.

hole relaxation to the InP core is diminished, which results in the observed superlinear increase and sublinear increase in the CdS and core-arm interface emission respectively as depicted in Figure 4c. For the onset of saturation in the InP/ZnS-CdS interface emission as the pump fluence is increased to $\langle N \rangle \sim 10$, the bleaching of X$_0$ and the corresponding decay of Y$_0$ occurs extremely fast, indicating that holes in CdS located close to the InP/ZnS core are sufficient to fully saturate its hole states. These TA results are consistent with the PL spectra and pump fluence dependent peak intensities in Figure 4a,c, where at this pump fluence, the Type II emission is fully saturated and CdS emission increases linearly. In contrast, for CdSe seeded CdS tetrapods excited at the same high pump fluence (*i.e.*, $\langle N \rangle \sim 10$), there is still a fast decay ($\sim$1.4 ps) for the transition in the CdS arm and a correspondingly slow rise for the transition in the CdSe core as revealed in Figure 5d, which indicates that the core hole states in CdSe have not been filled completely. This may be explained by the weaker driving force for hole relaxation into the CdSe core due to the smaller

valence band offset ($\sim$0.4 eV[31] as opposed to $\sim$0.8 eV in InP-CdS) at the interface between the CdSe core and CdS arm. In the case of the InP/ZnS seeded CdS tetrapods, the large valence band offset between the InP/ZnS core and CdS arms provided a large thermodynamic impetus for arm-to-core hole localization, allowing for fast saturation of the hole states in the core.

CONCLUSION

In conclusion, we have demonstrated that Type II InP/ZnS seeded CdS tetrapods can achieve MME of comparable intensities at relatively low pump fluence and pump-dependent color tunability over a wide range on the CIE diagram. When comparing with Type I CdSe seeded CdS tetrapods of approximately the same CdS arm dimensions, it was concluded that the efficient dual emission, high photostability and wide color tunability in the Type II tetrapods were due to the large valence band offset and suppressed Auger recombination. This work highlights the importance of band alignment in the achievement of highly efficient color-tunable MME in semiconductor nanoheterostructures.

EXPERIMENTAL SECTION

Structural Characterization. *Transmission Electron Microscopy (TEM).* A JEOL JEM 1220F (100 kV accelerating voltage) microscope

was used to obtain bright field TEM images of the nanoparticles. For TEM sample preparation, a drop of the nanoparticle solution was placed onto a 300 mesh size copper grid covered with a continuous carbon film. Excess solution was removed with an adsorbent paper,

and the sample was dried at room temperature. The high-resolution TEM images and detailed elemental analysis were carried out on a FEI Titan 80-300 electron microscope operated at 200 kV, which is equipped with an electron beam monochromator, an energy dispersive X-ray spectroscopy (EDX) and a Gatan electron energy loss spectrometer. The probing electron beam size for the EDX measurement was around 0.3 nm. The dwell time for each EDX spectrum was 10 s.

X-ray Diffraction (XRD). XRD data was obtained with a diffractometer (Bruker AXS, GADDS) using Cu Kα radiation ($\lambda = 1.540598$ Å) in the range of $20-100°$. Samples were prepared on a clean silicon wafer by placing drops of concentrated silica coated nanoparticles in hexane on the silicon surface and dried at 60 °C in the oven. This was repeated several times until a thin layer of solid was formed on the silicon substrate.

Optical Characterization. Absorption spectra were obtained with an Agilent 8453 UV−visible spectrophotometer in UV−visible range. Photoluminescence (PL) spectra in visible region and NIR region were collected with a spectrofluorometer and HORIBA Jobin Yvon Fluorolog 3 spectrometer equipped with liquid nitrogen cooled InGaAs photodiode detector, respectively. Time-resolved fluorescence data were obtained by using a NanoLED pulsed laser diode excitation source and a HORIBA Jobin Yvon TCSPC detection system FluoroHub. Care was taken to ensure that the concentrations of the core and core-seeded nanostructures were sufficiently dilute to avoid contributions from reabsorption or energy transfer. Absolute quantum yield measurement of the type II nanocrystals has been carried with a Hamamatsu Quantaurus-QY NIR model (C11347-12), which is suitable for measurements from 400 to 1100 nm.

The femtosecond laser source for the following optical measurements was a Coherent Legend Ti:sapphire regenerative amplifier (150 fs, 1 kHz, 800 nm) seeded by a Coherent Vitesse oscillator (100 fs, 80 MHz). For the fluence-dependent PL measurements, the solution samples in the 2 mm thick quartz cells were excited using 400 nm excitation pulses obtained by using a BBO doubling crystal. The time-integrated PL spectra were collected in a conventional backscattering geometry and detected by a charge-coupled device array (Princeton Instruments, Pixis 400B) coupled with a monochromator (Acton, Spectra Pro 2500i).

For pump−probe measurements, the solution samples in quartz cells were pumped by 400 nm pulses, which were focused onto a 200 μm spot and overlapped with white-light continuum probe pulses generated with a 1 mm thick sapphire plate (that was focused by a parabolic mirror to a spot of ~20 μm diameter). The differential transmission $[(T - T_0)/T_0]$ spectra of the samples were performed in a nondegenerate pump−probe configuration with chirp-correction (where T_0 is the transmission of probe beam without pump excitation of the sample and T is the transmission of the probe beam with pump excitation of the sample). The linear polarization of the pump pulse was adjusted to be perpendicular to that of the probe pulse with a polarizer and a half-wave plate. The cross-polarization helps to eliminate any contribution from coherent artifacts at early times. Pump-induced transmission changes were monitored using a monochromator/PMT configuration coupled to a lock-in amplifier. The pump beam was chopped at 83 Hz and used as the reference frequency for the lock-in amplifier.

REFERENCES AND NOTES

1. Han, M. Y.; Gao, X. H.; Su, J. Z.; Nie, S. Quantum-Dot-Tagged Microbeads for Multiplexed Optical Coding of Biomolecules. *Nat. Biotechnol.* **2001**, *19*, 631–635.

2. Jaiswal, J. K.; Mattoussi, H.; Mauro, J. M.; Simon, S. M. Long-Term Multiple Color Imaging of Live Cells Using Quantum Dot Bioconjugates. *Nat. Biotechnol.* **2003**, *21*, 47–51.

3. Resch-Genger, U.; Grabolle, M.; Cavaliere-Jaricot, S.; Nitschke, R.; Nann, T. Quantum Dots *versus* Organic Dyes as Fluorescent Labels. *Nat. Methods* **2008**, *5*, 763–775.

4. Goldman, E. R.; Clapp, A. R.; Anderson, G. P.; Uyeda, H. T.; Mauro, J. M.; Medintz, I. L.; Mattoussi, H. Multiplexed Toxin Analysis Using Four Colors of Quantum Dot Fluororeagents. *Anal. Chem.* **2004**, *76*, 684–688.

5. Medintz, I. L.; Uyeda, H. T.; Goldman, E. R.; Mattoussi, H. Quantum Dot Bioconjugates for Imaging, Labelling and Sensing. *Nat. Mater.* **2005**, *4*, 435–446.

6. Snee, P. T.; Somers, R. C.; Nair, G.; Zimmer, J. P.; Bawendi, M. G.; Nocera, D. G. A Ratiometric CdSe/ZnS Nanocrystal pH Sensor. *J. Am. Chem. Soc.* **2006**, *128*, 13320–13321.

7. Thakar, R.; Chen, Y. C.; Snee, P. T. Efficient Emission from Core/(Doped) Shell Nanoparticles: Applications for Chemical Sensing. *Nano Lett.* **2007**, *7*, 3429–3432.

8. Liu, W.; Howarth, M.; Greytak, A. B.; Zheng, Y.; Nocera, D. G.; Ting, A. Y.; Bawendi, M. G. Compact Biocompatible Quantum Dots Functionalized for Cellular Imaging. *J. Am. Chem. Soc.* **2008**, *130*, 1274–1284.

9. Thakar, R.; Chen, Y. C.; Snee, P. T. Efficient Emission from Core/(Doped) Shell Nanoparticles: Applications for Chemical Sensing. *Nano Lett.* **2007**, *7*, 3429–3432.

10. Lutich, A. A.; Mauser, C.; Da Como, E.; Huang, J.; Vaneski, A.; Talapin, D. V.; Rogach, A. L.; Feldmann, J. Multiexcitonic Dual Emission in CdSe/CdS Tetrapods and Nanorods. *Nano Lett.* **2010**, *10*, 4646–4650.

11. Galland, C.; Brovelli, S.; Bae, W. K.; Padilha, L. A.; Meinardi, F.; Klimov, V. I. Dynamic Hole Blockade Yields Two-Color Quantum and Classical Light from Dot-in-Bulk Nanocrystals. *Nano Lett.* **2013**, *13*, 321–328.

12. Manna, L.; Milliron, D. J.; Meisel, A.; Scher, E. C.; Alivisatos, A. P. Controlled Growth of Tetrapod-Branched Inorganic Nanocrystals. *Nat. Mater.* **2003**, *2*, 382–385.

13. Talapin, D. V.; Nelson, J. H.; Shevchenko, E. V.; Aloni, S.; Sadtler, B.; Alivisatos, A. P. Seeded Growth of Highly Luminescent CdSe/CdS Nanoheterostructures with Rod and Tetrapod Morphologies. *Nano Lett.* **2007**, *7*, 2951–2959.

14. Fiore, A.; Mastria, R.; Lupo, M. G.; Lanzani, G.; Giannini, C.; Carlino, E.; Morello, G.; De Giorgi, M.; Li, Y.; Cingolani, R.; Manna, L. Tetrapod-Shaped Colloidal Nanocrystals of II-VI Semiconductors Prepared by Seeded Growth. *J. Am. Chem. Soc.* **2009**, *131*, 2274–2282.

15. Kan, S.; Mokari, T.; Rothenberg, E.; Banin, U. Synthesis and Size-Dependent Properties of Zinc-Blende Semiconductor Quantum Rods. *Nat. Mater.* **2003**, *3*, 155–158.

16. Li, L.; Reiss, P. One-Pot Synthesis of Highly Luminescent InP/ZnS Nanocrystals without Precursor Injection. *J. Am. Chem. Soc.* **2008**, *130*, 11588–11589.

17. Ung, T. D. T.; Reiss, P.; Nguyen, Q. L. Luminescence Properties of In(Zn)P Alloy Core/ZnS Shell Quantum Dots. *Appl. Phys. Lett.* **2010**, *97*, 193104(1−3).

18. Ung, T. D. T.; Pham, T. T.; Nguyen, Q. L.; Li, L.; Reiss, P. Comparative Photoluminescence Study of Close-Packed and Colloidal InP/ZnS Quantum Dots. *Appl. Phys. Lett.* **2010**, *96*, 073102(1−3).

19. Lide, D. R. *CRC Handbook of Chemistry and Physics*, 82nd ed.; CRC Press, Inc.: Boca Raton, FL, 2001; pp 204−208.

20. Oladeji, I. O.; Chow, L. Synthesis and Processing of CdS/ZnS Multilayer Films for Solar Cell Application. *Thin Solid Films* **2005**, *474*, 77–83.

21. Dennis, A. M.; Mangum, B. D.; Piryatinski, A.; Park, Y. S.; Hannah, D. C.; Casson, J. L.; Williams, D. J.; Schaller, R. D.; Htoon, H.; Hollingsworth, J. A. Suppressed Blinking and Auger Recombination in Near-Infrared Type-II InP/CdS Nanocrystal Quantum Dots. *Nano Lett.* **2012**, *12*, 5545–5551.

22. Piryatinski, A.; Ivanov, S. A.; Tretiak, S.; Klimov, V. I. Effect of Quantum and Dielectric Confinement on the Exciton-Exciton Interaction Energy in Type II Core/Shell Semiconductor Nanocrystals. *Nano Lett.* **2007**, *7*, 108–115.

23. Wu, J. C.; Zheng, J. W.; Zacherl, C. L.; Wu, P.; Liu, Z. K.; Xu, R. Hybrid Functionals Study of Band Bowing, Band Edges

and Electronic Structures of $Cd_{1-x}Zn_xS$ Solid Solution. *J. Phys. Chem. C* **2011**, *115*, 19741–19748.

24. Htoon, H.; Malko, A. V.; Bussian, D.; Vela, J.; Chen, Y.; Hollingsworth, J. A.; Klimov, V. I. Highly Emissive Multiexcitons in Steady-State Photoluminescence of Individual "Giant" CdSe/CdS Core/Shell Nanocrystals. *Nano Lett.* **2010**, *10*, 2401–2407.

25. Kulakovskii, V. D.; Bacher, G.; Weigand, R.; Kummell, T.; Forchel, A.; Borovitskaya, E.; Leonardi, K.; Hommel, D. Fine Structure of Biexciton Emission in Symmetric and Asymmetric CdSe/ZnSe Single Quantum Dots. *Phys. Rev. Lett.* **1999**, *82*, 1780–1783.

26. Morello, G.; Fiore, A.; Mastria, R.; Falqui, A.; Genovese, A.; Creti, A.; Lomascolo, M.; Franchini, I. R.; Manna, L.; Della Sala, F.; Cingolani, R.; De Giorgi, M. Temperature and Size Dependence of the Optical Properties of Tetrapod-Shaped Colloidal Nanocrystals Exhibiting Type-II Transitions. *J. Phys. Chem. C* **2011**, *115*, 18094–18104.

27. Wang, C. H.; Chen, T. T.; Tan, K. W.; Chen, Y. F.; Cheng, C. T.; Chou, P. T. Photoluminescence Properties of CdTe/CdSe Core-Shell Type-II Quantum Dots. *J. Appl. Phys.* **2006**, *99*, 123521(1−4).

28. Chang, W. H.; Liao, Y. A.; Hsu, W. T.; Lee, M. C.; Chiu, P. C.; Chyi, J. I. Carrier Dynamics of Type-II InAs/GaAs Quantum Dots Covered by a Thin $GaAs_{(1-x)}Sb_{(x)}$ Layer. *Appl. Phys. Lett.* **2008**, *93*, 033107(1−3).

29. Garcia-Santamaria, F.; Chen, Y. F.; Vela, J.; Schaller, R. D.; Hollingsworth, J. A.; Klimov, V. I. Suppressed Auger Recombination in "Giant" Nanocrystals Boosts Optical Gain Performance. *Nano Lett.* **2009**, *9*, 3482–3488.

30. Oron, D.; Kazes, M.; Banin, U. Multiexcitons in Type-II Colloidal Semiconductor Quantum Dots. *Phys. Rev. B* **2007**, *75*, 035330(1−7).

31. Steiner, D.; Dorfs, D.; Banin, U.; Della Sala, F.; Manna, L.; Millo, O. Determination of Band Offsets in Heterostructured Colloidal Nanorods Using Scanning Tunneling Spectroscopy. *Nano Lett.* **2008**, *8*, 2954–2958.

ARTICLE